Launching deep subwavelength bulk plasmon polaritons through hyperbolic metamaterials for surface imaging with tuneable ultra-short illumination depth

Article *in* Nanoscale · October 2016

DOI: 10.1039/C6NR03313J

CITATIONS
8

READS
99

7 authors, including:

Weijie Kong
The institute of Optics and Electronics
33 PUBLICATIONS **272** CITATIONS
SEE PROFILE

Wenjuan Du
Xiangtan University
8 PUBLICATIONS **60** CITATIONS
SEE PROFILE

Zeyu Zhao
Fudan University
138 PUBLICATIONS **5,068** CITATIONS
SEE PROFILE

Nanoscale

PAPER

View Article Online
View Journal

Cite this: DOI: 10.1039/c6nr03313j

Launching deep subwavelength bulk plasmon polaritons through hyperbolic metamaterials for surface imaging with a tuneable ultra-short illumination depth†

Weijie Kong,‡[a] Wenjuan Du,‡[a,b] Kaipeng Liu,[a] Changtao Wang,[a] Ling Liu,[a] Zeyu Zhao[a] and Xiangang Luo*[a]

Received 23rd April 2016,
Accepted 1st September 2016

DOI: 10.1039/c6nr03313j

www.rsc.org/nanoscale

Hyperbolic metamaterials (HMMs) composed of multiple nanometal–dielectric films are proposed for launching deep subwavelength bulk plasmon polaritons (BPPs) as uniform, large area surface imaging illumination sources with a skin depth even beyond 10 nm. Benefiting from the coupled plasmon modes over a wide wavevector range in HMMs, the illumination depth could be continually tuned, simply by adjusting the incidence angle of light impinged on a grating structure for BPP excitation. As an example, the illumination depths of 19–63 nm at a light wavelength of 532 nm are demonstrated with SiO_2–Ag multifilms. Moreover, the structure holds its deep subwavelength illumination depth for a broad light wavelength range, resembling that of light total internal reflection in a prism with an ultra high refractive index. Furthermore, a fluorescent nanoparticle based micro-zone system was employed for estimating the illumination depth of the HMM structure. The method is believed to provide access for surface imaging features in ultra thin layers especially for bio-samples.

Introduction

Interfacial and near-surface events, such as the cell plasma membrane fusion of synaptic vesicles and the movement of single molecules during signal transduction,[1] are key components of physical and biological systems. These events occur in the plasma membrane orientation at a distance of tens of nanometers and even below.[2] In traditional fluorescence microscopy[3] as a common tool for imaging fluorophore-labeled biological samples, the entire samples are flooded with excitation light, and the images of the surface zone are easily deteriorated by the fluorescence excited outside the layer of interest. In order to reduce the unwanted light from internal samples and achieve the surface images of samples with high contrast, only the surface zone needs to be illuminated. Total internal reflection fluorescence microscopy (TIRFM),[4–7] also termed evanescent wave fluorescence microscopy, selectively excites the fluorescent labeled entities located near the surface. Two kinds of TIRFM illumination setups are usually employed in the form of a prism[8] and an immersion objective with a ring diaphragm,[9] respectively. Due to the high surface confinement of the illumination profile, the internal fluorescence of samples is inhibited and the contrast of the surface images of samples could be considerably improved.[6,10] Recently, Ramachandran *et al.*[11] presented a simple TIRFM structure by side illuminating a thin cover glass plate with LED light. In the above methods, the minimum depth, d_{min}, of illumination is mainly determined by the refractive index of a solid prism or immersion oil, on the interface of which bio-samples' light total internal reflection occurs. Due to the limitation of the available high refractive index, the d_{min} attained in experiments is approximately only 100–200 nm, implying the failure of good surface observation for weak signals in bio-activities confined within ultra-thin surface films, such as a cell membrane with a thickness of approximately 4–6 nm.[12–14]

To obtain a much smaller illumination depth, a dielectric film with hundreds of nanometer thickness and a high refractive index is proposed for evanescent wave illumination.[15–17] In this way, the leaked evanescent mode component outside the thin film as a waveguide is utilized for illuminating the surface zone of samples above it. Compared with prism and immersion objective illumination, a higher refractive index could be easily obtained for a thin film and help to yield a smaller depth.

[a]State Key Laboratory of Optical Technologies on Nano-Fabrication and Micro-Engineering, Institute of Optics and Electronics, Chinese Academy of Science, P.O. Box 350, Chengdu 610209, China. E-mail: lxg@ioe.ac.cn
[b]University of Chinese Academy of Sciences, Beijing 100049, China

† Electronic supplementary information (ESI) available: The AFM measured morphology image of the outermost Ag film of the multilayer structure, and the SEM images of the fluorescent nanoparticles above the outermost Ag film. See DOI: 10.1039/c6nr03313j

‡ These authors contributed equally to this work.

For example, a TiO_2 film (n = 2.5) delivers three discrete illumination depths of 39 nm, 25 nm and 19 nm for a variant side excitation grating period and a fixed laser light wavelength.[18]

Surface imaging could also be performed by employing surface plasmon polariton (SPP) illumination.[19–21] SPPs are electromagnetic excitations propagating at the dielectric/conductor interface, evanescently confined in the perpendicular direction, which have been employed for super resolution lithography[22,23] and other subwavelength electromagnetic applications.[24,25] When the light is coupled into the metal film by using a prism,[26] an optically matched microscopy objective lens[27] or diffraction gratings,[28] the SPPs near the surface of the metal film would be generated and the evanescent field is employed for illuminating samples with a small penetration depth. But it is hard to launch deep subwavelength SPP modes with a high transverse wavevector for the problem of associated great light absorption, thus the ultra-short illumination depth could not be achieved by a single metal film. Moreover, because of the weak suppression capability for electromagnetic modes outside the filtering window of a single metal film, the light modes with a low transverse wavevector would leak into SPP modes, which could worsen the surface images drastically.

For the illumination applications, the light intensity uniformity and the illumination area are considered. To realize uniform surface illumination, the key point is to launch the single evanescent wave mode and inhibit any other light modes in the same region. For a single metal film, multiple electromagnetic modes would be launched and thus the interference among them could result in a nonuniform illumination intensity, which is harmful for imaging. Furthermore, the limited area size for illumination would be encountered for both thin film waveguide and SPPs excited by a single metal film, mainly due to the light scattering and absorption loss as surface modes propagating transversally over the illumination area.

In this paper, we propose and demonstrate that deep subwavelength surface illumination imaging could be realized by launching the bulk plasmon polariton mode in hyperbolic metamaterials (HMMs) composed of multiple nanometal–dielectric films. The unique feature of HMMs for coupled super mode of excited free electrons oscillation in a volume space, instead of being confined in two dimensional spaces like SPPs,[29] help to support deep subwavelength evanescent waves and inhibit other light modes diffracted by excitation gratings.[25] This delivers a uniform and large area surface illumination field with an even sub-10 nm depth, a continually tuneable illumination depth obtained by simply adjusting the light incidence angle, and successful operation held in a wide light wavelength range. It is believed that this method helps to give a potential way for imaging nano cell plasma membranes and other samples with ultra-thin layers of interest *etc*.

Design and principles

The schematic of the BPP illumination structure employing HMM is presented in Fig. 1(a). A monochromatic plane wave in transverse magnetic (TM) polarization impinges from the substrate side upon a 1D grating close to HMM, which is composed of alternatively stacked metal–dielectric films. Instead of employing SPPs near the metal–dielectric interface, here bulk plasmon polaritons (BPPs)[30,31] existing in the entire bulk space of multifilms are launched and engineered to achieve an uniform and large area surface illumination field with an ultra-short illumination depth. The BPP modes, as the superplasmonic modes, are formed by the mutual coupling of plasmonic polariton fields between the adjacent metal–dielectric films. Furthermore, the BPP modes show propagation behaviors inside HMM and decay exponentially outside with dielectric medium. To further address this point, the effective medium theory (EMT)[32,33] is employed for treating the multifilms as an anisotropic medium, and the effective permittivities in the x, y and z directions are described as:

$$\varepsilon_x = \varepsilon_y = \varepsilon_d f + \varepsilon_m(1-f) \quad (1)$$

$$\varepsilon_z^{-1} = \varepsilon_d^{-1} f + \varepsilon_m^{-1}(1-f) \quad (2)$$

where ε_m and ε_d are the permittivities of metal and dielectric films, respectively. $f = h_d/(h_d + h_m)$ is the filling factor of dielectric films, h_m and h_d are the thicknesses of metal and dielectric films respectively. For TM polarization, the dispersion relation of light inside an anisotropic medium could be written as $k_x^2/\varepsilon_z + k_z^2/\varepsilon_x = k_0^2$, where k_x and k_z represent the wavevector components along the x- and z-direction, respectively; k_0 is the light wavevector under vacuum.

For instance, 8 pairs of alternatively stacked Ag–SiO_2 films and additional one Ag film constitute a HMM. The thicknesses of Ag and SiO_2 films are 20 nm and 80 nm, respectively. At a light wavelength of 532 nm, the permittivities for Ag and SiO_2 are $\varepsilon_{Ag} = -11.3 + 0.17i$,[34] and $\varepsilon_{SiO_2} = 2.13$,[35] respectively, and the calculated $\varepsilon_x = \varepsilon_y = -0.556 + 0.034i$, $\varepsilon_z = 2.794 + 0.002i$. The corresponding dispersion relation in EMT approximation is shown in Fig. 1(b) (red line). It is clear that the dispersion relation shows a hyperbolic shape, enabling propagation of light with an infinite large transverse wavevector through multifilms. For accurately describing the BPP modes inside multifilms, rigorous coupled wave analysis (RCWA)[36] is employed for calculating the OTF of HMMs, which exhibits a pair of symmetric profiles with high amplitude transmission for large transverse wavevectors within a fixed region,[37] as shown in Fig. 1(b) (blue line). In addition, due to the Fabry–Perot resonances inside HMMs, multiple peaks appear in the OTF.[38] Intuitively, but not rigorously, HMMs behave like an anisotropic medium with a very high refractive index, much larger than those normal optical materials. Compared with that of a single Ag film (green line), the HMM OTF shows a window filtering effect, which greatly inhibits the light modes outside the window benefiting from the strong coupling behaviour of BPPs inside the films. This feature plays a key role in BPP illumination with an ultra-short depth as would be seen below.

As light photons impinge the excitation grating, the generated diffraction waves with matched transverse momentum

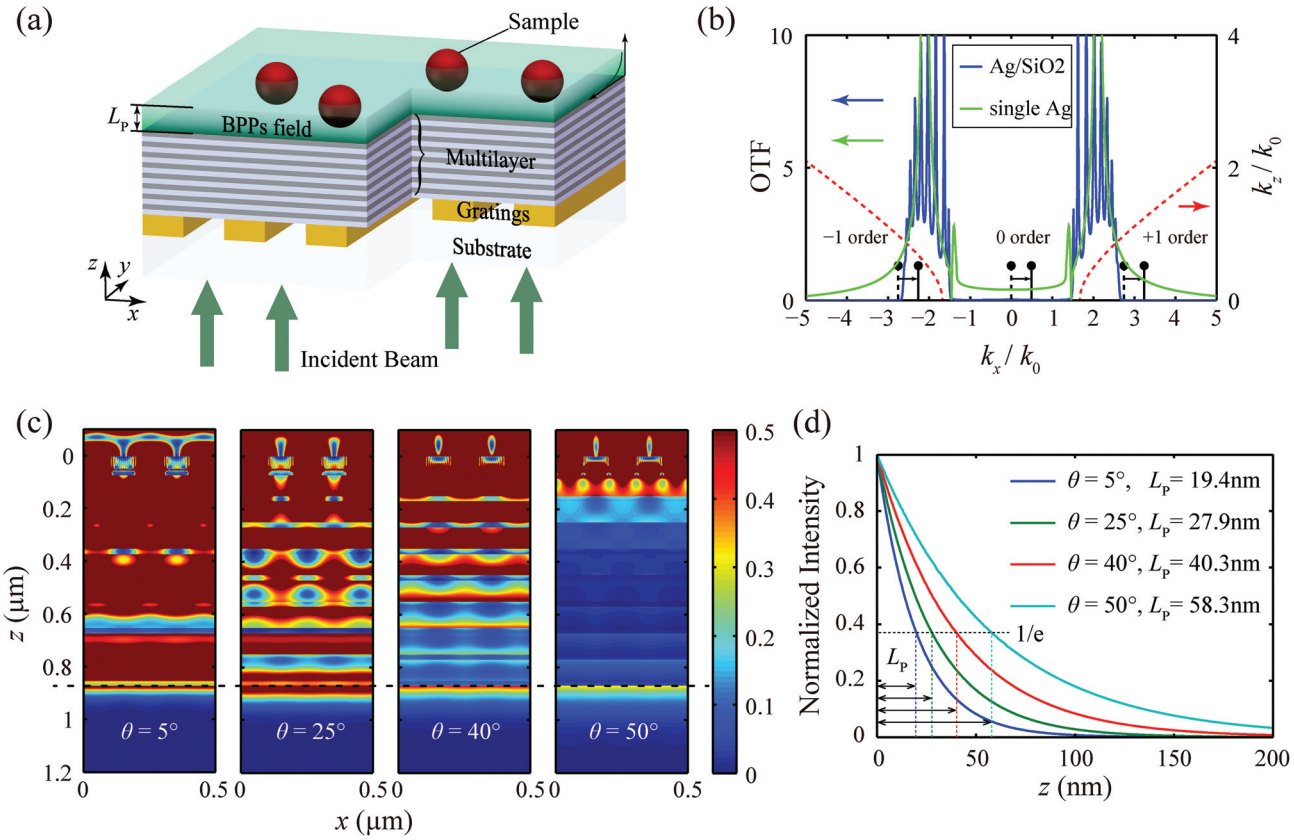

Fig. 1 (a) Schematic of the BPP illumination structure. (b) The optical transfer function (OTF) for the single Ag layer (green line) and Ag–SiO_2 multifilms (blue line). The red line represents the dispersion relation of Ag–SiO_2 multifilms in EMT approximation. (c) The optical intensity distributions in the x–z plane when incidence angles are 5°, 25°, 40° and 50°, respectively. (d) The corresponding intensity decay curves away from the illumination surface in (c).

would be coupled to the BPP modes. The illumination depth in the sample adjacent to HMMs, defined as the distance where the light intensity drops to $1/e$ of its value at the surface, could be described as

$$L_p = \frac{\lambda}{4\pi\sqrt{(k_{\mathrm{BPPs}}/k_0)^2 - \varepsilon}} = \frac{\lambda}{4\pi\sqrt{(n\sin\theta + q\lambda/d)^2 - \varepsilon}} \quad (3)$$

where λ and θ are the wavelength and incidence angle of excitation light, respectively, n is the refractive index of the substrate, ε is the permittivity of the illuminated sample, and q is the diffraction order. According to eqn (3), the illumination depth mainly depends on the incidence angle, wavelength as well as the permittivity of samples. Simply by controlling the incidence angle of light, the illumination depth could be continually tuned.

As an example, the grating period is set as 202 nm and the duty cycle and depth of Si grating are 0.5 and 50 nm, respectively. The permittivity of Si at 532 nm is calculated by interpolating the data from ref. 35, which is 16.98 + 0.37i. Fig. 1(c) plots the optical intensity distributions in x–z sections at different incidence angles. Obviously, the intensities outside the HMM decay drastically along the z direction. The decaying feature lessens with the increase of incidence angle and delivers the enlarged illumination depth correspondingly, as shown in Fig. 1(d). At the incidence angles of 5°, 25°, 40° and 50°, the corresponding illumination depths are 19 nm, 28 nm, 40 nm and 58 nm, respectively. For the sake of exciting only one BPP mode in HMM, the incidence angle is limited in the range of 0–51° to screen the other orders of light diffraction. The simulated depth coincides well with that calculated from eqn (3), as demonstrated in Fig. 2.

Results and discussion

Uniformity analysis of the illumination field

Unlike surface illumination with SPPs and dielectric waveguides, BPPs help to realize nearly uniform illumination over a large area where incidence light is uniform enough. The slight distortion of light uniformity mainly arises from the interference between BPP and propagation photon modes. The relationship between the nonuniformity factor ($U = (I_{\max} - I_{\min})/(I_{\max} + I_{\min})$) in the illumination region and the incidence angle is plotted in the top panel of Fig. 3, where $I_{\max}$ and $I_{\min}$ are the maximum and minimum intensities of the illumination field, respectively. It is clear from this figure that the nonuniformity factors are smaller than 0.1 except for at

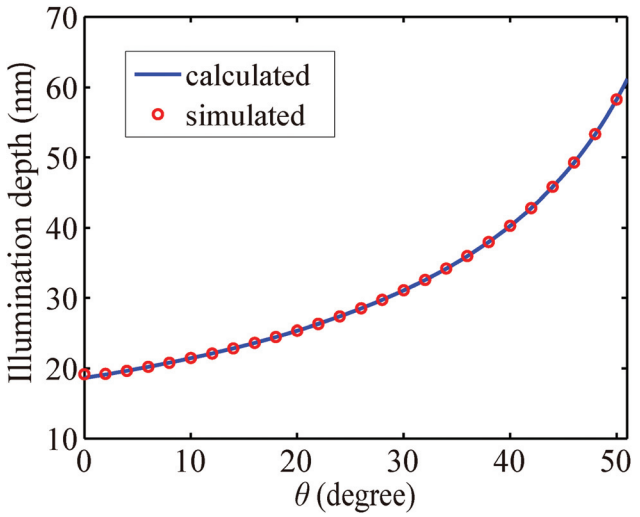

Fig. 2 Calculated and simulated illumination depths into aqueous solutions as a function of light incidence angle with a wavelength of 532 nm.

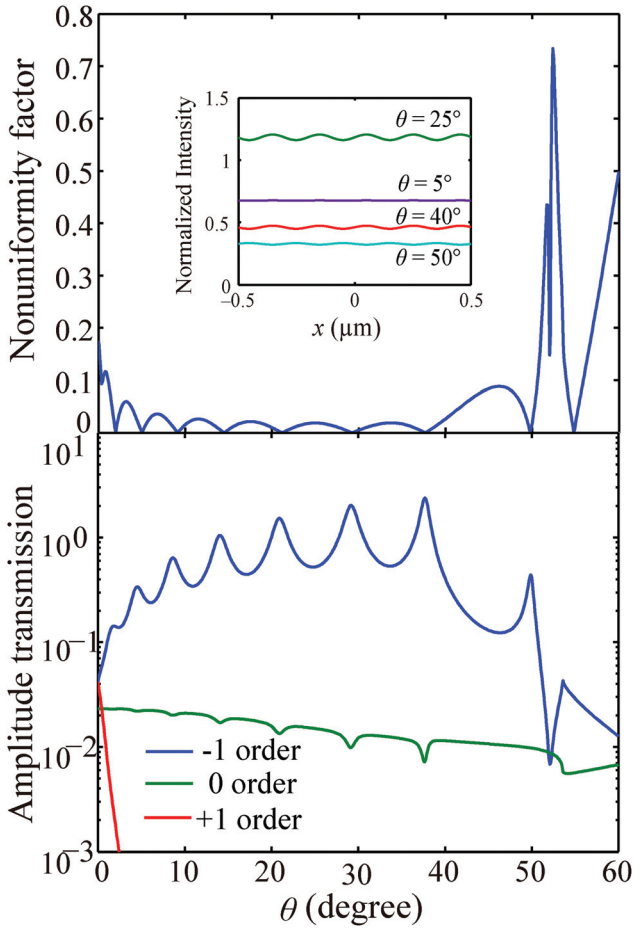

Fig. 3 Top panel is the nonuniformity factor in the BPP illumination surface of HMM at different incidence angles and the inset is the intensity profiles along the x direction in the illumination surface at 5°, 25°, 40° and 50°, respectively. The bottom panel is the amplitude transmission of 0, $\pm 1^{st}$ orders of diffraction light from grating at the different incidence angles.

the incidence angles around 0° and those larger than 51°, generating uniform illumination as illustrated by the insets of Fig. 3. This implies that incoherent light sources with large divergence could be used for BPP illumination as well, which is a unique advantageous ability in comparison with the TIRFM, dielectric and SPP waveguide film structure. At angles around 0° and larger than 51°, multiple BPP modes are excited and their interference contributes to the great increase of nonuniformity factor. Moreover, the nonuniformity factor varies with the incidence angle in an oscillation way. The main reason is related to the amplitude transmission of light through HMM, which shows multiple resonance peaks associated with its OTF, and that of 0^{th} order light is much flatter, as illustrated in the bottom panel of Fig. 3. The larger transmission amplitude of the -1^{st} order in BPP mode through HMM results in a relatively smaller perturbation from the 0^{th} order light and hence a smaller nonuniformity factor, and *vice versa*.

Performances in a wide wavelength range

As shown above, the surface illumination performance is mainly determined by the accessible k_x range of BPP mode, which could be clearly seen from both OTF calculations and dispersion relation contours in Fig. 4 with 400–700 nm light wavelength, for the same structure as that in Fig. 3. It is noteworthy that the OTF and effective k_z are normalized by $k_{nor} = 2\pi/t_p$ (t_p = 100 nm) instead of k_0 for visualising the broadening and shift of the filtering window. One can find that the Ag–SiO_2 film system shows two types of OTF profiles. For wavelengths larger than 530 nm, the OTF takes the form of a filtering window, in which BPP modes are supported inside films acting as HMMs with BPP modes with nearly zero imaginary part of k_z, indicating that BPPs propagate without significant loss. And the light modes outside the window are greatly inhibited with great imaginary k_z. The transmission window region could be defined as where the amplitude suppression ratio of the pass band to stop the band is larger than 20 and the amplitude transmission exceeds 0.015, for the good uniformity and large intensity of illumination. For the light wavelengths ranging between 400 nm and 530 nm, both BPP modes and normal photons with small k_x exist together, as demonstrated as well in the contours of dispersion relations in Fig. 4(b). From the viewing point of surface illumination, only the first type with strong window-like BPP modes is preferred.

The accessible k_x range of BPP mode and illumination depth shows strong dependence on the grating period and the k_x shift value defined by the light wavelength and incidence angle as well. To obtain uniform illumination, only one BPP mode is desired and the full width of the BPP window and light incidence angle 0–90° could not be always fully utilized with a fixed grating period for a tuneable depth range as large as possible, as illustrated in Fig. 5. For example, a d_{min} of ~19 nm is obtained for 532 nm wavelength, grating period 202 nm and an incidence angle around 0°, corresponding to ~2.63 k_0 at the upper window boundary. The maximum depth d_{max} of illumination occurs at the lower boundary 1.49 k_0 with

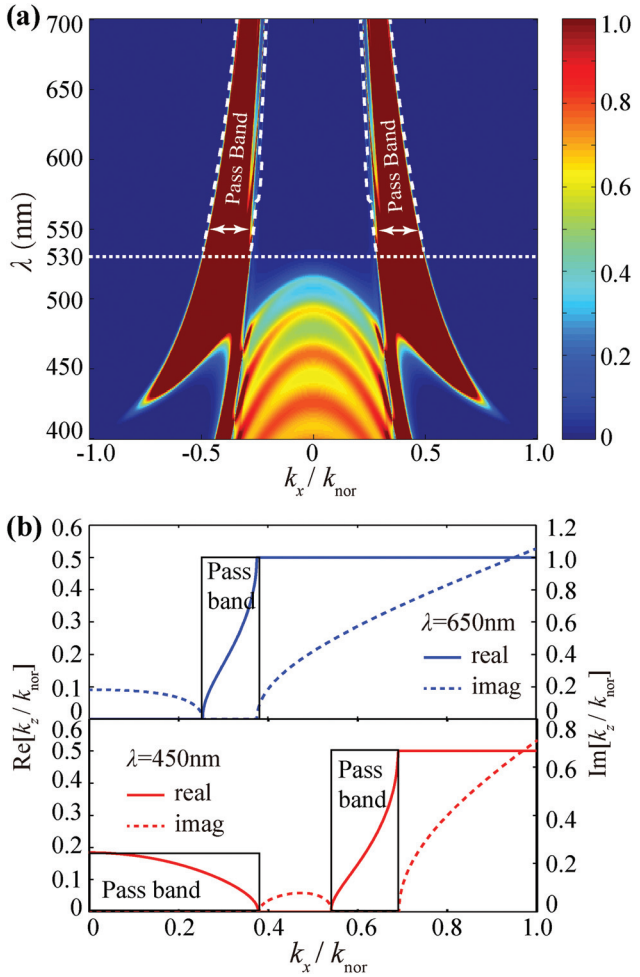

Fig. 4 (a) The OTF of HMM at different incidence wavelengths. (b) The real (real line) and imaginary part (dotted line) of k_z for variant k_x calculated in Bloch theorem[39–41] at 450 nm and 650 nm, respectively.

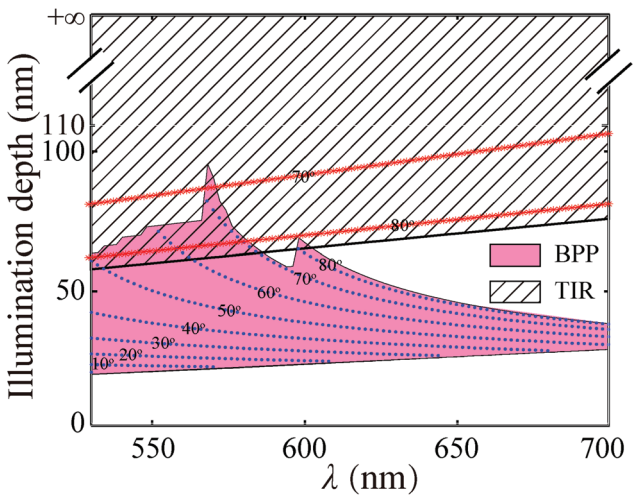

Fig. 5 Illumination depth in aqueous solutions for BPP and TIR illumination structures as a function of incidence wavelength. The blue and red dotted lines are contour lines of incidence angle θ in BPP illumination and TIR illumination, respectively.

~51° incidence. In the case of light wavelength 530 nm, d_{min} and d_{max} are nearly kept constant compared with counterparts at 532 nm wavelength. For a light wavelength of 700 nm, however, the attained d_{max} is only 37 nm at 2.0 k_0 and ~90° angle, not reaching the lower boundary due to the great shift of the window. The d_{min} in this case is 28 nm with 46° angle. Thus, surface illumination with a depth beyond 28 nm holds for a wide light wavelength ranging from 530 nm to 700 nm, provided that the incidence angle is smaller than 46°. Compared with the illumination depth range of TIRFM (red region drawn in Fig. 5) with the prism refractive index being 1.52, BPPs show dramatic shrinkage of the illumination depth just at a small light incidence angle, which is good for compact experimental setups. And at some specific wavelengths, 530–600 nm, the accessible illumination depth region intersects with that of TIRFM and the maximum tuneable depth extended to infinity could be realized here.

Influences of metal/dielectric film thickness

It is possible to design the BPP illumination feature by optimizing HMM parameters. For example, Fig. 6(a) plots the OTFs for variant dielectric filling factors of 0.6, 0.7 and 0.8, and the thickness t_p of the Ag–SiO_2 pair is fixed as those in Fig. 6(c). In this case, the OTF transmission window widens, and the lower k_x boundary is shifted to smaller absolute values for a large filling factor of 0.8. Thus, the available maximum illumination depth increases considerably to about 63 nm (Fig. 6(b)). The d_{min} does not change significantly, as the grating period and light wavelength are fixed here.

In another case shown in Fig. 6(c) with variant t_p values of 50 nm, 80 nm and 100 nm and fixed filling factor 0.8, the OTF window upper boundary increases greatly even to 0.82

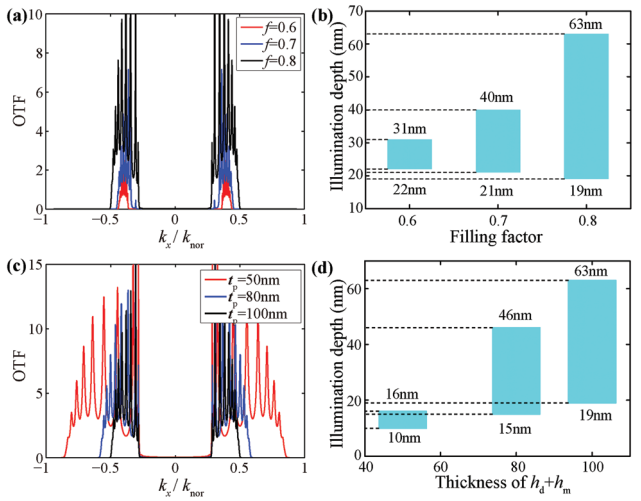

Fig. 6 (a) OTF and (b) corresponding illumination depths at different filling factors of dielectric (t_p = 100 nm). (c) OTF and (d) illumination depth at different thicknesses of Ag–SiO_2 film pair (f = 0.8). The incidence wavelength is 532 nm. The period of excitation grating is 202 nm for (b) and 173 nm for t_p = 80 nm and 120 nm for t_p = 50 nm in (c).

k_{nor} (4.50 k_0) for a smaller thickness due to the enhanced strong coupling between the two adjacent Ag films. So it would be possible to realize a much smaller illumination depth down to 20 nm for 80 nm Ag–SiO_2 pair thickness, and 10 nm for 50 nm thickness, as shown in Fig. 6(d) with a reduced excitation grating period. At the same time, the lower boundary remains nearly unchanged. This point could be well explained by the EMT analysis defined with eqn (1)–(2), which gives a good approximation for the dispersion relation profile with a lower BPP boundary $k_x \approx \sqrt{\varepsilon_z} k_0$. It is not surprising that the available maximum illumination depth drops greatly as well in Fig. 6(d). This occurs because some extra BPP modes would be generated for a large light incidence angle. This constraint results in a limited maximum illumination depth for a fixed grating period.

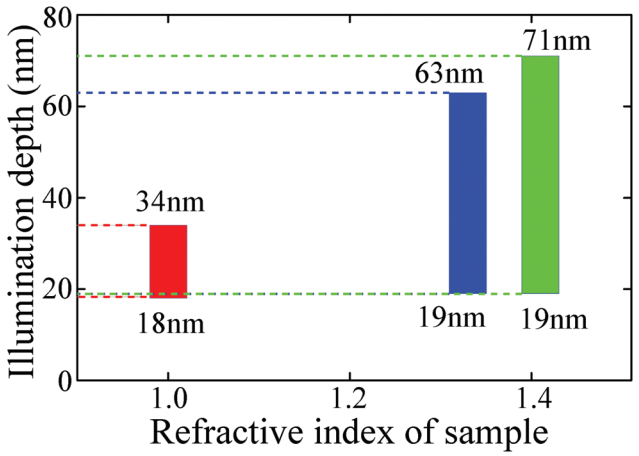

Fig. 7 Illumination depth of the BPP structure in air, aqueous solutions and PDMS, respectively. The incidence wavelength is 532 nm.

Influence of the refractive index of samples

The BPP illumination feature also depends on the refractive index of samples, as could be seen from eqn (3). Fig. 7 depicts the available illumination depth for three samples with air, aqueous solution and PDMS and the corresponding refractive index is 1.0, 1.33 and 1.41, respectively. The BPP structure is fixed here. First, the d_{min} in the three samples is nearly fixed to be about 18 nm for BPP excitation light with small incidence angles. This point could be well understood, considering that deep subwavelength BPP modes have so large k_x that the small sample's refractive index brings no significant influence. As the incidence angle increases and k_x decreases correspondingly, the BPP illumination depth grows much faster for samples with a high index. For instance, the d_{max} turns to be 63 nm and 71 nm for aqueous solutions and PDMS samples, over two times that in air. This may be good news in experiments in which both small d_{min} and a large tuneable range are preferred.

Nanoparticles imaging under the BPP illumination

In order to demonstrate the surface imaging capability of the BPP illumination structure, two crossed fluorescent nanoparticles with the radius of 100 nm are illuminated by the evanescent field with different decay depths (depicted in the inset of Fig. 8(b)). If emissive fluorescence is proportional to the local illumination intensity, the intensity of fluorescence in detecting the plane could be expressed as:

$$I_e(x) = \alpha \int_0^{2r} I_0 \exp(-y/L_p) S(x,y) \mathrm{d}y \qquad (4)$$

where α and r are the excitation factor of fluorescence and the radius of nanoparticles, respectively, I_0 and L_p are the initial illumination intensity and the decay depth of the evanescent field, respectively. Furthermore, $S(x,y)$ is the function describ-

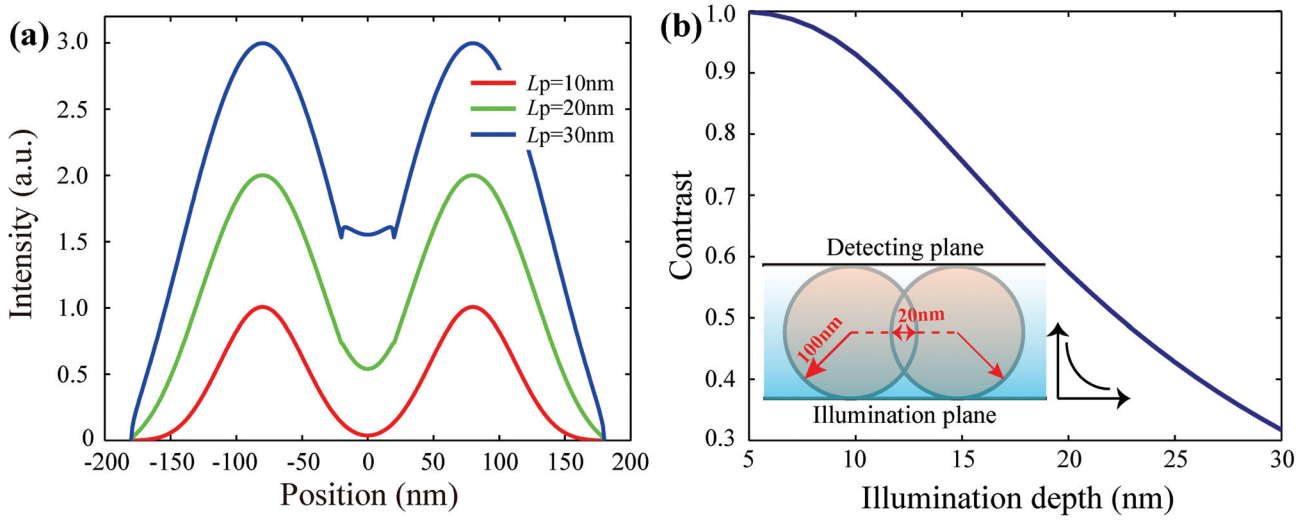

Fig. 8 (a) The calculated images of the crossed fluorescent nanoparticles obtained in the detecting plane (inset in (b)) under the illumination depth of 10 nm, 20 nm and 30 nm, respectively. (b) The contrast of nanoparticles' image as a function of illumination depth. The inset shows the schematic of nanoparticles imaging.

ing the area of two-dimensional nanoparticles, and the illumination direction is along the *y*-axis. Subsequently, the images of nanoparticles in the detecting plane are calculated and shown in Fig. 8(a). When the illumination depth is short, only the parts near the surface are illuminated, thus one can get the distinct image of each nanoparticle. As the illumination depth increases, the more illumination field penetrates into the crossed part of nanoparticles, and then the images of two nanoparticles start to merge, which reduces the contrast of the nanoparticles' image. Herein, the contrast is defined as $C = (I_{max} - I_{central})/(I_{max} + I_{central})$, where I_{max} and $I_{central}$ are the maximum intensity and the intensity located at the central position between nanoparticles along the detecting plane, respectively. Fig. 8(b) shows the relationship between contrast and illumination depth. It is obvious that the contrast decreases near-linearly with the illumination depth. It is worth noting that the contrast approaches unity when the illumination depth is near 5 nm and even smaller. This means that the short illumination depth guarantees the distinct and high contrast image for the surface part of the sample.

Experiment

The fabrication process of the BPP illumination structure is as follows: a 200 nm period Si grating was firstly fabricated on a silicon substrate by large area laser interference lithography and then transferred to another fused silica substrate with the planar surface by a template stripping method.[42] After that, 8 pairs of Ag (20 nm)–SiO_2 (80 nm) and additional one Ag layer (20 nm) are deposited alternatively on the planar Si grating surface by magnetron sputtering. The detailed fabrication steps could be seen from ref. 31 published by our group. Fig. 9(a) depicts the cross-section image of the fabricated illumination structure, and the main geometrical parameters approach to their design values. The atomic force microscopy (AFM) measured morphology image of a small part of the outmost Ag film is shown in the ESI, Fig. S1,† and the corresponding root-mean-square (RMS) surface roughness is about 2.3 nm. Based on the theoretical analysis from above, the 0^{th} diffraction light from grating should be inhibited for realizing the pure BPP illumination, which could be seen from Fig. 3. For the sake of confirming this, the efficiency of 0^{th} diffraction light through the illumination structure has been measured at different incidence angles on the silica substrate, as shown in Fig. 9(b). Obviously, the acquired efficiency is smaller than 6×10^{-4} throughout in the range of 0–45°. Although the measured efficiencies at small incidence angles could not reach the predicted ones ($\sim 5 \times 10^{-5}$) owing to rough films' scattering, the real efficiency is sufficient to inhibit the 0^{th} diffraction light from the BPP wave.

In order to characterize the illumination depth of the BPP illumination structure, a micro-zone fluorescence system[18] consisting of fluorescent nanoparticles deposited on the illumination area was applied. The fluorescent nanoparticles with a radius of 20 nm have the excitation and emission wavelengths of 540 nm and 560 nm, respectively (F-8792 Invitrogen™). The nanoparticles were firstly diluted in deionized (DI) water and then 5 μL of nanoparticle solution was dropped on the illumination surface of a multilayer structure and it was allowed to dry naturally. For the sake of clearing away the suspended nanoparticles and leaving only stable ones, the original multilayer structure with nanoparticles was further rinsed with DI water. Finally, this structure was dried again. The scanning electron microscopy (SEM) images of the obtained fluorescent nanoparticles above the outermost Ag film of the multilayer structure are shown in ESI, Fig. S2.† It is clear that many isolated nanoparticles appear on the Ag film, which is expected in following experiments.

When setting up the micro-zone fluorescence system, the multilayer structure with fluorescent nanoparticles was placed

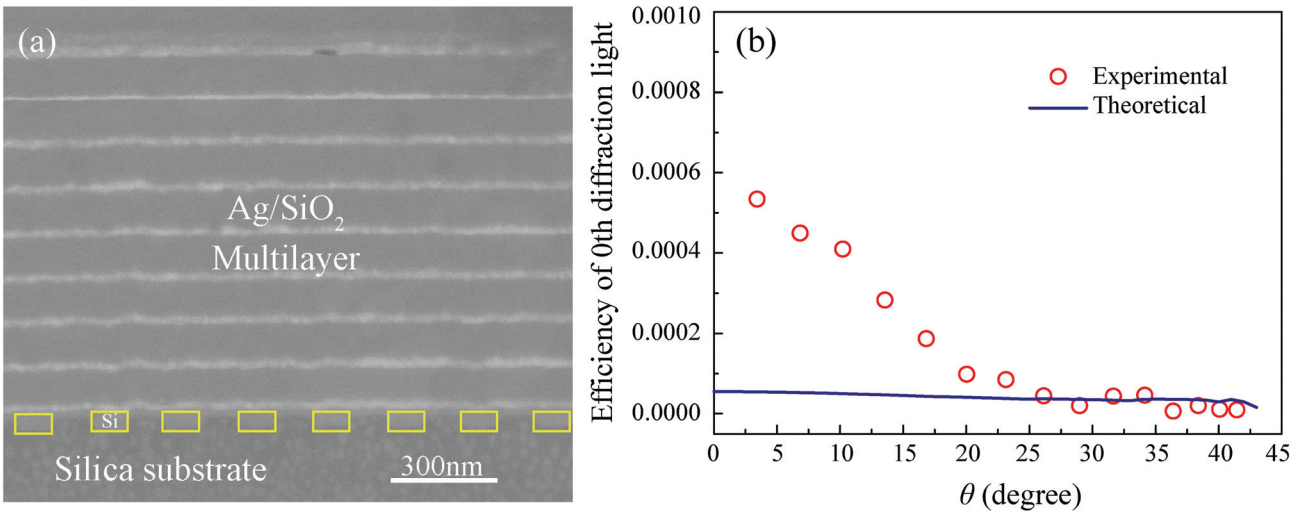

Fig. 9 (a) The SEM cross-section image of the BPP illumination structure. (b) The efficiency of the 0^{th} diffraction light from grating through the illumination structure as a function of the incidence angle in the silica substrate.

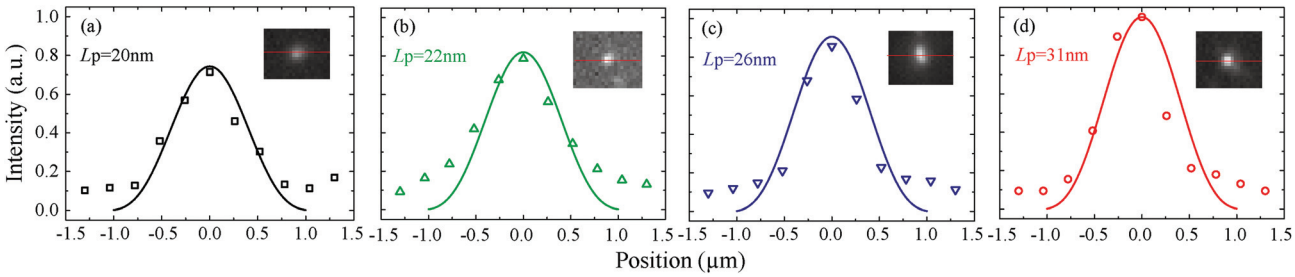

Fig. 10 The experimental and calculated cross-section intensity of a single fluorescent nanoparticle (radius 20 nm), at the different incidence angles of (a) 10°, (b) 20°, (c) 30° and (d) 40°, respectively. The insets are the images of fluorescent nanoparticles.

on the stage of an upright microscope assembled with a Motic objective (40×, NA 0.65) and an intensity-sensitive CCD detector (PIXIS 1024 Princeton Instruments Corp., 13 × 13 μm pixel size). The excitation laser with a power of 5.9 mW (532 nm CW, SDL-532-100T, Shanghai Dream Lasers Technology Corp.) was installed under the multilayer structure, and the light strikes on the subwavelength grating of the BPP illumination structure at different incidence angles. Meanwhile, a notch filter (NF533-17, center wavelength 533 nm, band width 17 nm, ThorLabs Corp.) was fixed on the objective to eliminate the possible excitation laser from the emission fluorescence. Through focusing on one single nanoparticle, the corresponding images could be captured by using a CCD detector, which are shown in the insets of Fig. 10.

The dots in Fig. 10 show the cross-sectional intensity of a single nanoparticle extracted from the captured images at different incidence angles of 10°, 20°, 30° and 40°, respectively. The predicted illumination depths are 20 nm, 22 nm, 26 nm and 31 nm, respectively. Due to the different evanescent intensities on the illumination surface of the multilayer structure when tuning the incidence angle (shown in the inset in Fig. 3), the cross sectional intensities were firstly normalized by their corresponding initial evanescent intensity in the illumination surface. After that, the obtained intensities were further normalized to the maximum intensity with the illumination depth of 31 nm (Fig. 10(d)) for comparing them with the calculated results. Under the conditions of the same evanescent intensity on the illumination surface of the structure, and the linear dependence of the fluorescence on the local optical power, the longer illumination depth could result in a higher fluorescence intensity.

For obtaining the calculated intensity profiles of a single fluorescent nanoparticle, the following calculation method[18] could be used. The optical intensity above the illumination structure could be expressed as $I(z) = I_0 \exp(-z/L_p)$. While, the image of fluorescent nanoparticles follows the expected form: $\mathrm{Image}(x,y) = \alpha\int[I(z)G(x,y,z)]^{*}P(x,y)\mathrm{d}z$, where α denotes the excitation factor of fluorescence, $G(x,y,z)$ describes the volume of nanoparticles, $P(x,y)$ is the point spread function (PSF) of the optical imaging system, and * represents the convolution operator. The PSF of the microscopy objective could be expressed as the Airy disk, which has the form of $I_0(2J_1(r)/r)^2$, where J_1 is the first-order Bessel function of the first kind, and r is the scaled distance from the center of the Airy disk for letting the first order diffraction ring lie at the distance $0.61\lambda/\mathrm{NA}$, where λ and NA are the fluorescence wavelength and the numerical aperture of the microscopy objective, respectively. Finally, similar to the experimental cases, the calculated intensity profiles were normalized to the maximum value with an illumination depth of 31 nm, which are plotted in solid lines in Fig. 10. It is clear that the normalized fluorescence intensity profiles obtained from calculations are overall in agreement with the measured ones for each incidence angle. This means the real illumination depth is just around the predicted one.

The difference between the measured and calculated intensity profiles is acceptable, which is mainly attributed to the negative impact of the films' roughness. Moreover, as expected, the peak intensity of the fluorescent nanoparticle improves with the increasing illumination depth. For the large evanescent field decay depth (>100 nm), the valid measurement of decay depth could be done by attaching a fluorescent nanoparticle to an AFM tip.[11]

Conclusions

In conclusion, we designed the BPP illumination structure with the HMM composed of metal–dielectric films for uniform and large area surface imaging with even 10 nm depth penetration. Simply by adjusting the incidence angle of light impinging on the BPP excitation grating, the illumination depth could be continually tuned. For the Ag–SiO_2 films' HMM structure, the illumination depths in the range of 19–63 nm in aqueous samples are achieved at a light wavelength of 532 nm. Also, the surface illumination feature holds well for a wide light wavelength range. Fluorescent nanoparticles were illuminated by the HMM structure at different incidence angles, and the corresponding fluorescence profiles were compared with the calculated ones for estimating the illumination depths. In addition, only a one dimensional excitation grating structure is employed in this paper, and the extension to two dimensional grating cases is available and would help to engineer the direction of excited BPPs for observing anisotropic samples. This work is believed to

provide a simple and valuable way to image events occurring in ultra thin layers down to a few nanometers with greatly improved contrast.

Acknowledgements

This work was supported by the 973 Program of China (no. 2013CBA01700) and the National Natural Science Foundation of China (no. 61505217 and 61138002).

References

1 S. E. Sund, J. A. Swanson and D. Axelrod, *Biophys. J.*, 1999, **77**, 2266–2283.
2 J. A. Steyer and W. Almers, *Nat. Rev. Mol. Cell Biol.*, 2001, **2**, 268–275.
3 J. W. Lichtman and J.-A. Conchello, *Nat. Methods*, 2005, **2**, 910–919.
4 D. Axelrod, *Traffic*, 2001, **2**, 764–774.
5 D. S. Johnson, J. K. Jaiswal and S. Simon, *Curr. Protoc. Cytom.*, 2012, 12.29. 11–12.29. 19.
6 L. Wang, C. Vasilev, D. P. Canniffe, L. R. Wilson, C. N. Hunter and A. J. Cadby, *Opt. Express*, 2012, **20**, 3311–3324.
7 D. Toomre and D. J. Manstein, *Trends Cell Biol.*, 2001, **11**, 298–303.
8 A. L. Stout and D. Axelrod, *Appl. Opt.*, 1989, **28**, 5237–5242.
9 T. P. Burghardt, A. D. Hipp and K. Ajtai, *Appl. Opt.*, 2009, **48**, 6120–6131.
10 C. M. Ajo-Franklin, L. Kam and S. G. Boxer, *Proc. Natl. Acad. Sci. U. S. A.*, 2001, **98**, 13643–13648.
11 S. Ramachandran, D. A. Cohen, A. P. Quist and R. Lal, *Sci. Rep.*, 2013, **3**, 2133.
12 V. Ruta, J. Chen and R. MacKinnon, *Cell*, 2005, **123**, 463–475.
13 S. H. White, A. S. Ladokhin, S. Jayasinghe and K. Hristova, *J. Biol. Chem.*, 2001, **276**, 32395–32398.
14 M. Gandhavadi, D. Allende, A. Vidal, S. Simon and T. McIntosh, *Biophys. J.*, 2002, **82**, 1469–1482.
15 B. Agnarsson, S. Ingthorsson, T. Gudjonsson and K. Leosson, *Opt. Express*, 2009, **17**, 5075–5082.
16 H. Grandin, B. Städler, M. Textor and J. Vörös, *Biosens. Bioelectron.*, 2006, **21**, 1476–1482.
17 A. Hassanzadeh, M. Nitsche, S. Mittler, S. Armstrong, J. Dixon and U. Langbein, *Appl. Phys. Lett.*, 2008, **92**, 233503.
18 H. Shen, E. Huang, T. Das, H. Xu, M. Ellisman and Z. Liu, *Opt. Express*, 2014, **22**, 10728–10734.
19 B. Rothenhäusler and W. Knoll, *Nature*, 1988, **332**, 615–617.
20 G. Stabler, M. Somekh and C. See, *J. Microsc.*, 2004, **214**, 328–333.
21 K. Watanabe, K. Matsuura, F. Kawata, K. Nagata, J. Ning and H. Kano, *Biomed. Opt. Express*, 2012, **3**, 354–359.
22 X. Luo and T. Ishihara, *Appl. Phys. Lett.*, 2004, **84**, 4780–4782.
23 J. Luo, B. Zeng, C. Wang, P. Gao, K. Liu, M. Pu, J. Jin, Z. Zhao, X. Li, H. Yu and X. Luo, *Nanoscale*, 2015, **7**, 18805–18812.
24 M. Pu, X. Li, X. Ma, Y. Wang, Z. Zhao, C. Wang, C. Hu, P. Gao, C. Huang, H. Ren, X. Li, F. Qin, M. Gu, M. Hong and X. Luo, *Sci. Adv.*, 2015, **1**, e1500396.
25 X. Luo, *Sci. China: Phys., Mech. Astron.*, 2015, **58**, 594201.
26 J. S. Shumaker-Parry and C. T. Campbell, *Anal. Chem.*, 2004, **76**, 907–917.
27 B. Huang, F. Yu and R. N. Zare, *Anal. Chem.*, 2007, **79**, 2979–2983.
28 B. K. Singh and A. C. Hillier, *Anal. Chem.*, 2006, **78**, 2009–2018.
29 K. V. Sreekanth, A. De Luca and G. Strangi, *Sci. Rep.*, 2013, **3**, 3291.
30 I. Avrutsky, I. Salakhutdinov, J. Elser and V. Podolskiy, *Phys. Rev. B: Condens. Matter*, 2007, **75**, 241402.
31 G. Liang, C. Wang, Z. Zhao, Y. Wang, N. Yao, P. Gao, Y. Luo, G. Gao, Q. Zhao and X. Luo, *Adv. Opt. Mater.*, 2015, **3**, 1248–1256.
32 S. Tretyakov, *Analytical modeling in applied electromagnetics*, Artech House, 2003.
33 S. A. Ramakrishna, J. Pendry, M. Wiltshire and W. Stewart, *J. Mod. Opt.*, 2003, **50**, 1419–1430.
34 M. D. Thoreson, Z. Liu, U. K. Chettiar, P. Nyga, A. V. Kildishev, V. P. Drachev, M. V. Pack and V. M. Shalaev, Sandia Report SAND2009-7034, Sandia National Laboratories, United States, 2010, vol. **41**, pp. 1–68.
35 E. D. Palik, *Handbook of optical constants of solids*, Academic press, 1998.
36 M. Moharam and T. Gaylord, *J. Opt. Soc. Am. B*, 1981, **71**, 811–818.
37 Z. Guo, Z. Zhao, L. Yan, P. Gao, C. Wang, N. Yao, K. Liu, B. Jiang and X. Luo, *Appl. Phys. Lett.*, 2014, **105**, 141107.
38 X. Li, S. He and Y. Jin, *Phys. Rev. B: Condens. Matter*, 2007, **75**, 045103.
39 J. Yang, X. Hu, X. Li, Z. Liu, X. Jiang and J. Zi, *Opt. Lett.*, 2010, **35**, 16–18.
40 J. Schilling, *Phys. Rev. E: Stat. Phys., Plasmas, Fluids, Relat. Interdiscip. Top*, 2006, **74**, 046618.
41 B. Wood, J. Pendry and D. Tsai, *Phys. Rev. B: Condens. Matter*, 2006, **74**, 115116.
42 X. Zhu, Y. Zhang, J. Zhang, J. Xu, Y. Ma, Z. Li and D. Yu, *Adv. Mater.*, 2010, **22**, 4345–4349.